Chemical Geology 707 (2026) 123312

Contents lists available at ScienceDirect

Chemical Geology

journal homepage: www.elsevier.com/locate/chemgeo

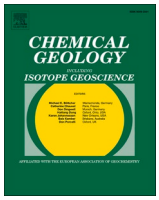

Research Paper

Assessing rare earth (yttrium) speciation in natural ores and processed waste streams using X-ray absorption spectroscopy

Anthony Boxleiter [a,*,1], Yinghao Wen [b,1], Martin Yan Hei Li [c], Joell Ashcraft [a], Yuanzhi Tang [b], W. Crawford Elliott [a]

[a] Department of Geosciences, Georgia State University, 38 Peachtree Center Avenue, Atlanta, GA 30303, United States
[b] School of Earth and Atmospheric Sciences, Georgia Institute of Technology, 311 Ferst Drive, Atlanta, GA 30332, United States
[c] Department of Earth Science and Engineering, Imperial College London, London SW7 2AZ, United Kingdom

ARTICLE INFO

Editor: Dr. Karen Johannesson

Keywords:
Rare earth elements
Granite-regolith
Bauxite-kaolin
Synchrotron X-ray absorption spectroscopy
Ion-exchange
Extractability

ABSTRACT

Rare earth elements (REE) are essential for advanced technologies and energy security. Understanding REE occurrences and speciation is critical for developing resource extraction technologies for diverse feedstocks. This study evaluated the speciation of yttrium (Y) in three types of natural ores and their processed waste streams using synchrotron X-ray absorption spectroscopy (XAS). The study materials included: Type-1 (granite-regolith ore), Type-2 (bauxite-kaolin ore), and Type-3 (sand fractions from processed bauxite-kaolin ore). Both Type-1 and Type-2 materials were kaolinite-rich and showed strong correlations between the fraction of adsorbed Y, predicted by linear combination fitting of the XAS data, and measured ion-exchangeable Y from assay. Adsorbed Y species (kaolinite and ferrihydrite) were the dominant Y speciation in Type-1 materials, which substantially decreased from 88.7–89.5% to 33.7–37.0% after the ion-exchange experiment. Similarly, the adsorbed Y species also decreased from 52.5–61.8% to 20.4–26.5% in Type-2 materials. The non-exchangeable fractions were primarily associated with Y-bearing phosphates and Y-bearing zircon in Type-2 materials. On the other hand, Type-3 materials were clay-deficient and showed drastically different Y speciation. Y-bearing phosphates accounted for the majority (~80–97%) of the Y speciation, including Y-bearing xenotime (~53–78%) and Y-bearing monazite (~16–30%). These associations highlighted the inherent variability in Y extractability from multi-mineral assemblages typical of these natural ores and their process waste streams containing both Y-bearing clays and non-clay phases. Considering the usefulness of treating Y as a proxy for predicting the behavior of other heavy REE (HREE), future advances in HREE extraction technologies can be achieved by combining mineralogical observations with insights from XAS analyses.

1. Introduction

Rare earth elements (REE: Sc, Y and La—Lu) are critical mineral resources vital for many important modern technologies and products (Long et al., 2010). Examples include neodymium (Nd) used in permanent magnets for electric vehicles and wind turbines, as well as yttrium (Y) used in metal alloys, visual displays, and laser systems (Van Gosen et al., 2019). Prior to manufacturing of these and other technologies using REE, mineral resources are mined from highly weathered crustal rocks such as regolith-hosted or lateritic deposits in East Asia, in addition to well-known hard rock deposits such as Mountain Pass and Bayan Obo (e.g., Li and Zhou, 2020; Li et al., 2017; Sanematsu and Watanabe, 2016; Bao and Zhao, 2008). REE are released from host minerals (e.g. phosphates, carbonates) and redistributed by solutions within regolith through "lateritic weathering" processes acting on parent rocks (Verplanck, 2017; Xu et al., 2017). REE ions are effectively sorbed onto mineral surfaces from these weathering solutions through outer-sphere and/or inner-sphere complexation reactions (Borst et al., 2020; Maurice, 2009; Langmuir, 1997).

Typically, regolith-hosted ion-adsorbed REE deposits contain large fractions of their REE enrichments associated with clay-rich assemblages. They are therefore often referred to as ion-adsorption clay (IAC) deposits (Beard et al., 2025; Li et al., 2017). Within IAC deposits, ion-sorbed REE comprise >50% of the total REE inventory (Liang et al.,

* Corresponding author.
E-mail address: aboxie@ymail.com (A. Boxleiter).
[1] Equal contribution.

https://doi.org/10.1016/j.chemgeo.2026.123312
Received 15 December 2025; Received in revised form 12 February 2026; Accepted 18 February 2026
Available online 19 February 2026

2025; Li et al., 2019, 2020; He et al., 2016; Ruan et al., 2005). Clay minerals (kaolinite and halloysite, in particular) are major sorbents for the REE in the regolith-hosted REE deposits (Li and Zhou, 2020, 2023). Lower fractions of the REE are also associated with other secondary minerals such as iron-oxyhydroxides (Wang et al., 2021; Chasse et al., 2019). IAC deposits are mined for their large portions of highly extractable REE (e.g., Brahim et al., 2022; Borst et al., 2020; Long et al., 2020; He et al., 2016; Xiao et al., 2015; Moldoveanu and Papangelakis, 2012, 2013, 2016). These deposits represent more than 80% of the global supply of mined heavy REE (HREE; Van Gosen et al., 2019; Li et al., 2017; Yang et al., 2013; Ruan and Jun, 2011; Wu et al., 1990, 1996).

While many economically significant deposits are found in East Asia, sedimentary-hosted resources with similar REE enrichment style are found in the Southeastern U.S. associated with the Piedmont Province and Upper Coastal Plain. Ion-exchangeable REE and secondary REE-phosphate minerals have been identified in the Piedmont regolith associated with granitic bedrocks (Cheshire et al., 2018; Bern et al., 2017). Significant REE enrichments were also found in kaolinite-rich strata of the Upper Coastal Plain formed initially by the transport and deposition of siliciclastic sediments sourced from weathered Piedmont Province rocks. The kaolin ore deposits also contained secondary REE-bearing phosphate minerals (crandallite and florencite; Cheshire et al., 2018). These secondary REE-phosphate minerals pointed to the redistribution of REE from detrital grains present in the original siliciclastic sediments building out the Coastal Plain during the late Mesozoic to Cenozoic eras (Boxleiter and Elliott, 2023; Cheshire et al., 2018; Cheshire, 2011). Chemical weathering processes mobilized REE from and within these kaolinite-rich, sedimentary deposits in the Upper Coastal Plain. REE were accumulated as ion-sorbed clays within strata underlying the weathered bauxite zones in these deposits (e.g., Andersonville mining district; Boxleiter et al., 2024).

Taken together, these ion-sorbed clays in the Upper Coastal Plain are potential REE resources in the U.S. These findings opened questions regarding the total speciation of REE in the kaolinite-rich strata. The REE in these sedimentary rocks are likely derived from the mixture of potential mineral carriers, including ion-adsorbed clays, associated with different fractions: clay-rich (raw) fractions, clay-rich (ion-exchange treated) fractions, and non-clay fractions. Therefore, the testable hypotheses in this study were focused on determining the breakdown of REE speciation for each of these fractions in order to determine their contribution to the whole rock.

These hypotheses are: (1) the raw, clay-rich fraction contains the highest proportion of surface-bound (ion-adsorbed) REE associated with kaolinite-clay content; and, (2) residues from ion-exchange treatment of raw samples, as well as the non-clay fraction, contain the highest proportion of lattice-bound (crystal structure) REE associated with primary or inherited detrital minerals. These hypotheses were tested using synchrotron X-ray absorption spectroscopy (XAS). This technique was notable and utilized as an in-situ, element-specific approach suitable for low concentration elements in complex heterogenous matrices.

Recent studies showed that kaolinite and other clay minerals could be identified as sorbents for REE using XAS-based techniques, (Bishop et al., 2024; Borst et al., 2020). These studies showed the nature of the molecular-scale interactions between REE and mineral surfaces as inner and/or outer sphere sorbed species. However, these studies were based on data measured from pure and/or lab-doped reference compounds. Few studies to our knowledge have translated XAS-based characterization techniques to natural ore samples with multi-mineral assemblages (clay and non-clay minerals), such as though in regoliths and clastic sedimentary rocks.

In this study, linear combination fitting (LCF) of XAS data in conjunction with mineralogy and geochemistry results were used to determine the relative percent of the speciation for Y – a representative proxy for HREE – in three types of samples derived from regolith-hosted and sedimentary-hosted IAC ores deposits in East Asia and the southeastern U.S., respectively. The insight gained from this approach provided a more comprehensive understanding of the occurrences and speciation of Y in these highly weathered materials, as well as their associated waste byproducts. An understanding of the characteristic heterogeneity and speciation of Y, and, more broadly all REE, provides insights for possible strategies and technologies for the extraction of these critical mineral resources from mined ores and their gangue fractions (mine waste tailings).

2. Materials and methods

2.1. Sample materials

Clay-rich (kaolinite and/or halloysite-dominated) granite-regolith from southeastern China, as well as sedimentary bauxite-kaolin ores and their sand-size fractions from the bauxite-kaolin ores of the southeastern U.S. were chosen for this study (Fig. 1). These three different types of study materials are described in detail below and in Table 1.

Granite-regolith ores (Type-1). The Type-1 materials are regolith samples containing 50–70% ion-exchangeable REE. They were collected and studied from the Zudong deposit, Jiangxi Province, South China (Li et al., 2019). The Type-1 material is composed of clay-rich (kaolinite and/or halloysite-dominated) regolith overlying weathered bedrocks including granites and similar crystalline rocks in southeast China. These regoliths are considered world-class IAC reserves for ion-exchangeable REE having significant fractions of the HREE (Y, Tb—Lu).

Bauxite-kaolin ores (Type-2). Clay-rich, bauxite-kaolin ore samples were collected and studied from geologic drill core (5 cm diameter core) from the Andersonville mining district, western Georgia, Upper Coastal Plain (Boxleiter et al., 2024). The samples were composed of 0.75 m length intervals of core (dried, crushed, split, and milled) collected from a depth of 12 to 21 m below surface. The section was typical of the bauxite-kaolin deposit type which can be found throughout the Andersonville district, as well as eastern Alabama (Eufaula district) and central Georgia (Wilkinson County). These deposits are characterized by three major zones: an upper kaolin zone, a middle bauxite zone, and a lower kaolin zone. Weathering processes mobilized and fractionated REE in these sections to form REE accumulations as IAC at the base of the bauxite zone and underlying the bauxite zone (Boxleiter et al., 2024).

Sand fractions, bauxite-kaolin ores (Type-3). Sand-size fractions were separated from the clay-rich, whole rock samples of bauxite-kaolin collected from core (Wilkinson County, central Georgia; Ashcraft, 2025). These gangue (sand) fractions are typically discarded during processing of mined kaolin ores and are predominantly comprised of non-clay minerals (quartz, Fe-sulfide, Ti-minerals, zircon, monazite, xenotime, and other heavy-minerals; Ashcraft et al., 2025). An additional sample of the sand-size fraction from the Buffalo Creek Member of the Cretaceous Gaillard Formation was studied. The Buffalo Creek Member represents a prominent kaolin lithology and major minable unit in the Sandersville district, which is part of the Georgia kaolin belt, but located just east of the bauxite-kaolins mined from the Wilkinson County district. The Buffalo Creek kaolins and other lithologies in the Sandersville district generally lack any bauxite formation. The Buffalo Creek Member was studied alongside the bauxite-kaolin samples because it is comparable in age and mineral content to the lower kaolin zones of the bauxite-kaolin deposits.

2.2. Mineralogy and geochemistry characterization

The mineralogy and geochemistry of the XAS study samples were referenced from their parent studies: Type-1 materials (Li et al., 2019); Type-2 materials (Boxleiter et al., 2024); and, Type-3 materials (Ashcraft, 2025). In these parent studies, X-ray diffractometry (XRD) was used to identify the major minerals present. The XRD data was accompanied by scanning electron microscopy (SEM) data for mineral ID confirmation. The elemental compositions of major/minor, trace, and

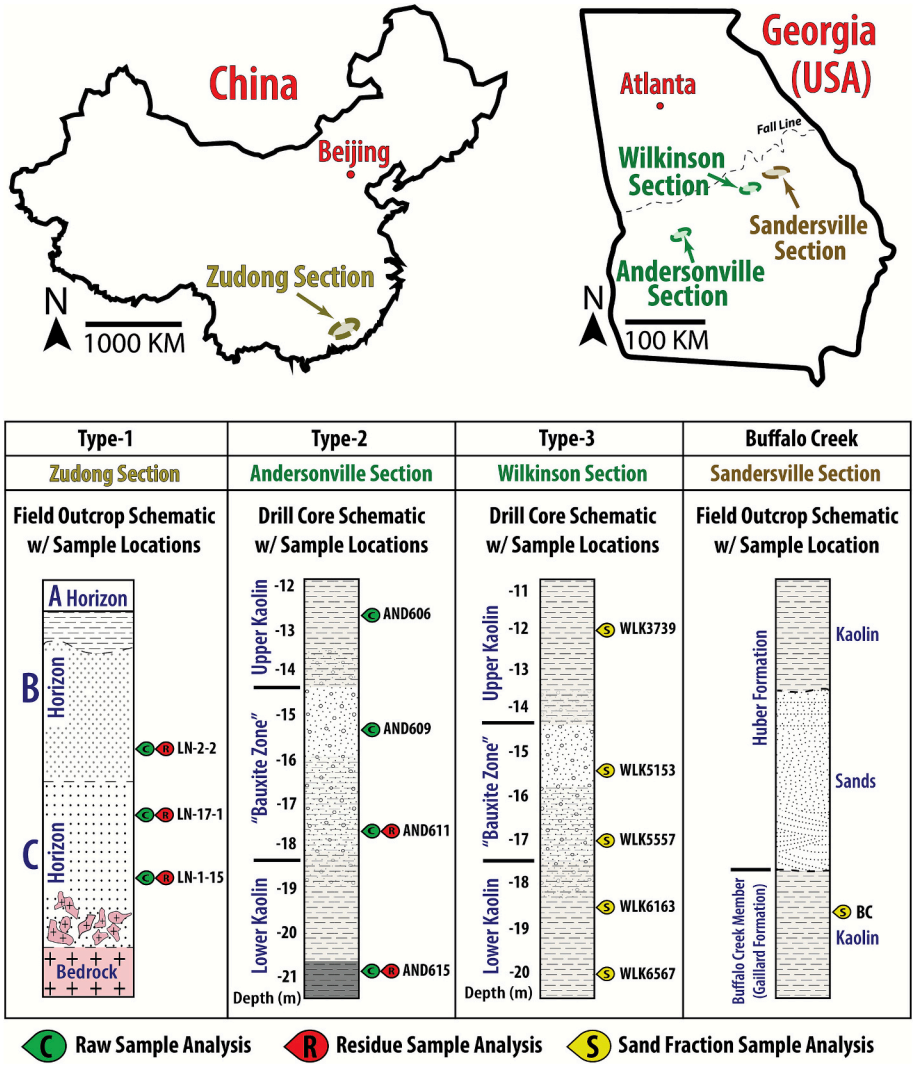

Fig. 1. Sampling locations for the original sample reference IDs used in this study.

REE were determined using a combination of X-ray fluorescence (XRF) and inductively coupled plasma optical emission and mass spectrometry (ICP-OES/MS; Activation Laboratories Ltd., Ontario, Canada, and ALS Chemex, Guangzhou, Co.). Listed in the Table 2 are the summarized mineralogy and major/minor oxide geochemistry of the XAS study samples per their parent study ("Reference ID").

The clay-rich Type-1 and Type-2 materials were fractioned into whole rock and residue fractions following the ion-exchange treatments using magnesium-sulfate solutions (Boxleiter et al., 2024). The residues of the Type-1 and Type-2 materials following ion-exchange treatment showed no changes in mineralogy or major/minor oxide composition. Minor amounts of Mg uptake in the Type-2 materials were noted due to the use of magnesium-sulfate solutions. Type-3 materials were fractioned into sand-size, heavy fractions by dispersing the mineral powders with sodium carbonate and sodium hexametaphosphate in water to produce a mineral grain slurry. Sand and silt-clay fractions were separated by physical screening of the slurry using an ASTM 325 mesh screen while rinsing with deionized water (see Text S1 in the Supplementary Information). The sand-size fractions were further separated into heavy and light mineral fractions by dense liquid separations using lithium tungstate (LMT or LST, ρ = 2.85–2.95 g/mL; see Text S2). Quartz is a non-REE-bearing mineral and typically predominant in the coarse fractions of mined kaolins (Elliott et al., 2018). The quartz (~2.65 g/cm^3) was separated from the coarse fractions to concentrate potential REE-bearing heavy-minerals (ρ >2.95 g/cm^3), therefore, producing a more REE-concentrated "heavy fraction" (HF) for XAS analyses. Residual light minerals (kaolinite, quartz) were found in the heavy fractions in varying amounts due to particles agglomerating and other effects which contribute to imperfect separations using dense liquids.

2.3. Synchrotron X-ray spectroscopy and microscopy analyses

2.3.1. XAS analysis

Bulk X-ray absorption near-edge structure (XANES) spectra of Y K-edge were collected at Beamline 6-BM at National Synchrotron Light Source (NSLS-II) in Brookhaven National Laboratory (Upton, NY) and Beamline 11–2 at Stanford Synchrotron Radiation Lightsource (SSRL) in the SLAC National Accelerator Laboratory (Menlo Park, CA). Fine-ground sample powders were mounted onto acrylic sample holders and sealed with Kapton tape for data collection in fluorescence mode. XANES spectra were collected with an edge energy of 17,038.4 eV. $Y_2(CO_3)_3$ was used for energy alignment. Multiple scans (4–6) were collected for each sample, depending on Y concentration and data quality.

Y was used as a representative proxy for the HREE. Y was conducive for approximating the behavior of other HREE (e.g. Dy, Ho) due to similar charge and ionic radius (Taggart et al., 2018; Bunzli, 2013; Tanaka et al., 2008). Y also presented an analytical advantage for

Table 1
Labeling and descriptions of the study materials. Samples from each deposit type represented different ore zones. For example, G1/G3 and G5/G6 represent a deeper sampling (~19.8–20.4 m below surface) and shallower sampling (~18.6–19.2 m below surface), respectively, from the lower kaolin zone. G7 and G8 represent a shallower and deeper sampling, respectively, from within the bauxite zone. Abbreviations: "AND" – Andersonville, GA, mining district; "WILK" – Wilkinson County, GA, mining district; "SH" – settled heavy fraction of mineral grains <45 μm in size. "HF" – heavy mineral fraction of mineral grains >45 μm in size; References: Li et al., 2019 (Type-1 materials); Boxleiter et al., 2024 (Type-2 materials); and, Ashcraft, 2025(Type-3 materials).

	XAS ID	Description of Sample	Reference ID
Type-1	LN-2-2	Lower B horizon, granite-regolith	LN-2-2
	LN-17-1	Upper C horizon, granite-regolith	LN-17-1
	LN-1-15	C horizon, granite-regolith	LN-1-15
Type-2	K1	Bottom of bauxite zone (raw)	AND 611
	K2	Bottom of bauxite zone (residue)	AND 611
	K3	Lignitic lower kaolin zone (raw)	AND 615
	K4	Lignitic lower kaolin zone (residue)	AND 615
	K5	Top of bauxite zone (raw)	AND 609
	K6	Upper kaolin zone (raw)	AND 606
Type-3	G1	Lower kaolin zone	WILK 6567 HF
	G3	Lower kaolin zone	WILK 6567 SH
	G5	Lower kaolin zone	WILK 6163 SH
	G6	Lower kaolin zone	WILK 6163 HF
	G7	Bauxite zone	WILK 5153 HF
	G8	Bauxite zone	WILK 5557 HF
	G10	Upper kaolin zone	WILK 3739 HF
	G11	Buffalo Creek Member (Gaillard Formation)	BC HF

detection because it was typically the most abundant HREE in the types of material used in the study (Boxleiter and Elliott, 2023; Elliott et al., 2018). Y was known to be associated with minerals such as Y-adsorbed kaolinite, Y-bearing phosphates (xenotime, monazite), and zircon in highly weathered materials (e.g. Ashcraft, 2025; Boxleiter et al., 2024; Li et al., 2019).

2.3.2. Micro X-ray fluorescence (μ-XRF) mapping and μ-XANES analysis

μ-XRF coupled with μ-XANES analyses were performed at Beamline 2–3 at SSRL. These coupled analyses were used for Type-3 materials which were characterized as both bulk powder samples (macro-scale) and mounted grain specimens (micro-scale). The mounted grain specimens were prepared as epoxy-embedded thin sections. Bulk XANES and μ-XANES analyses complemented each other to provide a more comprehensive view of spatially resolved elemental speciation and distribution.

The bulk and micro-scale speciation of Y may differ from each other, especially for natural samples due to their complex systems and the ore deposits they are found in. Interactions between Y-bearing minerals and the weathering processes occurring in ore deposits produce many geochemically distinct micro-environments. Discrete, localized differences in Y-bearing phases, such as secondary crystal overgrowths, may not be detectable in bulk powder sample measurements by XANES if they occur at low relative percentages (typical error range for μ-XANES and LCF is ~10%). For example, crystal overgrowths of xenotime were known to be found in association with detrital zircon grains in some Type-3 materials (Boxleiter and Elliott, 2023). The representativeness of μ-XANES/μ-XRF analyses is important to note due to the subjectivity of randomly selected areas for scanning regions of interest (ROI) from thin-sections, at the micron-level (Wen et al., 2025; Liu et al., 2019).

Coarse μ-XRF mapping was conducted for Y at 17200 eV with 100 μm step sizes and 20–25 ms dwell times. Coarse mapping was utilized to generate heat maps for rapid identification of regions of interest (ROI) containing particles of interest (POI; Fig. S6). Fine mapping was conducted from these ROI with 5–20 μm step sizes and 25–50 ms dwell times. These settings were varied per sample to produce effective resolution of the various sizes of particles across samples. Subsequent μ-XANES point analyses (1–5 μm spot size) were aimed at these particles to elucidate the differences in μ-XANES patterns for Y-speciation of individual mineral grains and their contribution to the bulk mixtures.

2.3.3. Model compounds

Fourteen Y model compounds were used in LCF modeling to interpret the XANES results in this study, which represent major Y-bearing mineral phases in natural samples (Fig. 2). Descriptions on the preparation of these model compounds can be found in our previous paper (Wen et al., 2025).

3. Results

3.1. Y model compounds

The Y K-edge XANES spectra displayed different spectral features for the 14 model compounds studied, reflecting the unique coordination environments for Y in these phases (Fig. 2). Their spectra were gathered into three groups (Figs. S1–S3). The first group of spectra show a strong absorption peak at around 17,056 eV, followed by a clear shoulder at ~17,066 eV and a broad bimodal hump centered at ~17,108 eV (Fig. S1). This group includes Y-bearing monazite and xenotime, which are very similar to each other, except for the relative intensity of the two overlapping peaks in the broad hump. This group also includes Y-bearing zircon, with the intensities of the shoulder and the two overlapping peaks in the hump all higher than those in monazite and

Table 2
Summarized mineralogy and major/minor oxide geochemistry of the three study materials derived from their parent studies: Li et al., 2019 (Type-1 materials); Boxleiter et al., 2024 (Type-2 materials); and, Ashcraft, 2025 (Type-3 materials).

	ID		Summarized Mineralogy					Summarized Major/Minor Oxide Geochemistry							
	XAS ID	Reference ID	Kaolinite-group	Gibbsite	Muscovite & illite	Quartz	Feldspar	SiO_2	Al_2O_3	TiO_2	K_2O	Fe_2O_3	P_2O_5	LOI	Sum others
Type-1	LN-2-2	LN-2-2	15%	ND	8%	66%	11%	75.6%	14.9%	<0.1%	2.7%	1.0%	<0.1%	4.4%	0.1%
	LN-17-1	LN-17-1	6%	ND	25%	49%	20%	72.1%	16.0%	<0.1%	4.2%	1.1%	<0.1%	4.4%	0.7%
	LN-1-15	LN-1-15	No data	No data	No data	No data	No data	74.2%	15.3%	<0.1%	4.3%	1.3%	<0.1%	3.7%	0.1%
Type-2	K1	AND 611	72%	26%	<1%	<1%	ND	32.6%	45.3%	2.0%	<0.1%	0.7%	<0.1%	19.2%	<0.1%
	K3	AND 615	93%	1%	<1%	<1%	ND	43.7%	36.5%	1.7%	0.2%	1.1%	<0.1%	15.9%	<0.1%
	K5	AND 609	31%	67%	<1%	<1%	ND	11.6%	55.5%	2.5%	<0.1%	0.4%	0.1%	28.9%	<0.1%
	K6	AND 606	81%	17%	<1%	<1%	ND	35.9%	42.1%	1.8%	0.1%	0.9%	0.1%	18.0%	<0.1%
Type-3	G1-G10	WILK HF	Mixture of heavy minerals: Ti-minerals (ilmenite, rutile), zircon, phosphates (monazite, xenotime), Fe-sulfides (pyrite, marcasite), and trace others, as well as residual light fraction minerals (kaolinite, gibbsite, mica, etc.)					No data							
	G11	BC HF													

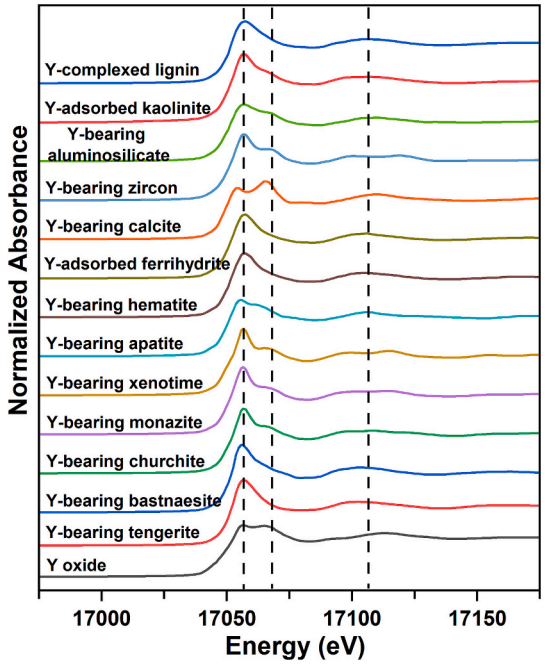

Fig. 2. Bulk XANES Y K-edge spectra of model compounds used in LCF (dashed lines in all Y XANES spectra indicate the energy positions of the main absorption peak at ~17,056 eV, shoulder at ~17,066 eV, and hump centered at ~17,108 eV).

xenotime.

The second group includes Y-bearing apatite and calcite, and Y oxide. The spectrum of Y-bearing apatite contains a weak absorption peak at ~17,056 eV, followed by a shoulder and a hump that are both at higher energies (Fig. S2). A doublet with similar peak intensities was observed at ~17,056 eV for Y-oxide. The peak at ~17,056 eV and its hump are shifted to a slightly higher energy relative to Y-bearing apatite. For Y-bearing calcite, the shoulder was markedly stronger than the main absorption peak, and the hump was centered at ~17,108 eV.

The third group (Y-bearing hematite, Y-adsorbed kaolinite, Y-adsorbed ferrihydrite, Y-complexed lignin, and Y-bearing bastnaesite) typically exhibit a clear and strong single peak feature at ~17,056 eV and a broad hump at ~17,108 eV, without any significant shoulder (Fig. S3). In particular, the spectra of Y-bearing hematite, Y-adsorbed ferrihydrite, and Y-complexed lignin are almost identical, except for the relative intensities of their main absorption peaks. The spectrum of Y-bearing bastnaesite displays a stronger main absorption peak than other model compounds in this group, a lower valley between the peak and the hump, and a hump that was slightly shifted to a lower energy.

The first- and second-derivatives for XANES spectra of the third group were plotted with normalized μ(E) in order to distinguish their highly similar spectral characteristics (Fig. S4). The first- and second-derivatives enhanced spectral resolution and highlighted subtle changes in coordination structures, which reveal differences that are not distinguishable in the original μ(E). However, these differences are primarily qualitative and do not directly translate into improved quantitative results of LCF. In common practice of XANES analysis, the derivatives are typically used to aid spectral comparison and interpretation, while LCF is performed using the normalized absorption spectra. LCF assumes linear additivity of absorption coefficients, which is mathematically not rigorous for the derivatives. In addition, performing LCF using derivatives may amplify high-frequency noise and increase the risk of overfitting features that are visually apparent but not necessarily chemically meaningful.

XANES analysis and LCF rely on mathematical fitting of features in the absorption spectra to determine the best-fit combination of model compounds. It is inherently challenging to identify the relative fractions of model compounds with highly similar local bonding environments and/or spectra features. Hence, other complementary analytical mineralogy techniques (e.g., XRD, SEM) and good knowledge of sample's composition are crucial for addressing the intrinsic limitations of LCF and to obtain a comprehensive understanding of Y speciation in the studied materials.

3.2. *Type-1 granite-regolith samples from South China*

Ion-exchange experiments were performed on three granite-regolith samples from China (LN-2-2, LN-1-17, and LN-1-15) to evaluate the extractability of Y, following similar procedures as previously reported (Boxleiter et al., 2024). The tabulated LCF results for raw samples (before ion-exchange) were compared with results for residue samples (after ion-exchange, Table 3). The Y K-edge bulk XANES spectra of these raw Type-1 materials and their ion-exchange residues are overlaid and shown in Fig. 3a. The XANES spectral of all three raw samples display a clear and strong single-peak feature at ~17,056 eV and a broad hump at ~17,108 eV. The spectra of the three Type-1 materials are almost identical, as can be observed in their overlaid spectra (Fig. S5). However, the XANES spectra of the ion-exchange residues show a markedly weaker absorption peak at ~17,056 eV and a flatter hump at ~17,108 eV, as well as a noticeably stronger shoulder at ~17,066 eV (Fig. 3a). Y species in raw samples were dominated by Y adsorbed on kaolinite (~41–65%) and ferrihydrite (~24–49%). These contents were readily leached as shown by the LCF model results for ion-exchange residues (Fig. 3, Table 3). The remaining Y species in raw samples were Y-bearing phosphate and Y-bearing carbonate phases.

3.3. *Type-2 whole rock bauxite-kaolin samples*

Ion-exchange experiments were performed on raw bauxite-kaolins samples (K1, K3, and K5) to evaluate the extractability of Y (Boxleiter et al., 2024). The highest percentages of extractable Y were found in the raw sample from the base of the bauxite zone (noted as K1) and the lignitic lower kaolin zone (noted as K3). The tabulated LCF results for raw samples were compared with their residues (Table 4). Y speciation for sample K1 included ~50% Y-adsorbed kaolinite and ~ 50% Y-bearing phosphates (i.e. the sum of 21.5% Y-bearing monazite, 10.4% Y-bearing xenotime, and 15.9% Y-bearing apatite). However, the fraction of Y-adsorbed kaolinite decreased sharply to ~20% in the ion-exchange residue (noted as K2). Most of the adsorbed Y species were extracted during ion-exchange with $MgSO_4$ with remaining non-exchangeable Y associated with monazite and other phosphates (Fig. 4). Monazite, for example, can be seen in the XANES spectrum of K2 as a clear shoulder at ~17,066 eV and the bimodal feature of the hump at ~17,108 eV (Fig. S1), whereas the spectrum for K1 was dominated by Y-adsorbed kaolinite observed as a single-peak feature at ~17,056 eV (Fig. 4a, Fig. S3).

The raw sample from the lignitic lower kaolin zone (noted as K3) contained 56.3% of Y as Y-adsorbed kaolinite, with remaining portions as 16.7% xenotime, 14.3% Y-bearing hematite, and 12.8% zircon. Similarly, a markedly lower fraction of Y-adsorbed kaolinite (26.5%) was shown for sample K4 (the residue of K3, Fig. 4). Note that the shoulder at ~17,066 eV in the XANES spectrum of K4 was not as obvious as the shoulder in K2 (Fig. 4a). This was likely because the sum of Y-adsorbed kaolinite and Y-bearing hematite still accounted for a substantial fraction (~50%) of the remaining Y in K4, giving rise to the stronger single-peak feature at ~17,056 eV. Comparatively, the ion-exchange residue sample K2 showed only ~20% sum contents of remaining Y-adsorbed kaolinite and therefore greater expression of a shoulder at ~17,066 eV attributed to the insoluble phases such as monazite (see Fig. S3).

In the raw sample from the top of the bauxite zone (noted as K5), Y is predominantly associated with monazite (42.7%), apatite (30.7%),

Table 3
Bulk XANES Y speciation of Type-1 materials determined by LCF (errors in parentheses).

Sample	Bulk Y (ppm)	Y speciation%						
		Adsorbed Y species		Y-bearing phosphates			Sum	R-Factor
		Y-adsorbed kaolinite	Y-adsorbed ferrihydrite	Y-bearing xenotime	Y-bearing apatite	Y-bearing calcite		
LN-2-2 raw	410	65.3 (2.9)	23.5 (1.9)	11.1 (0.8)			99.9	0.0003586
LN-2-2 residue	241	21.6 (1.6)	15.4 (1.4)	23.5 (1.5)	39.8 (2.3)		100.3	0.0003207
LN-17-1 raw	484	40.7 (1.9)	48.8 (2.3)	5.5 (0.5)		4.9 (0.8)	99.9	0.0001748
LN-17-1 residue	164	15.2 (1.2)	18.5 (1.3)	21.6 (1.5)		44.5 (2.7)	99.8	0.0004415
LN-1-15 raw	530	53.6 (2.5)	35.1 (2.1)	11.2 (0.8)			99.9	0.0002964
LN-1-15 residue	185	17.5 (0.8)	16.4 (0.7)	28.6 (1.4)	37.2 (1.4)		99.7	0.0003532

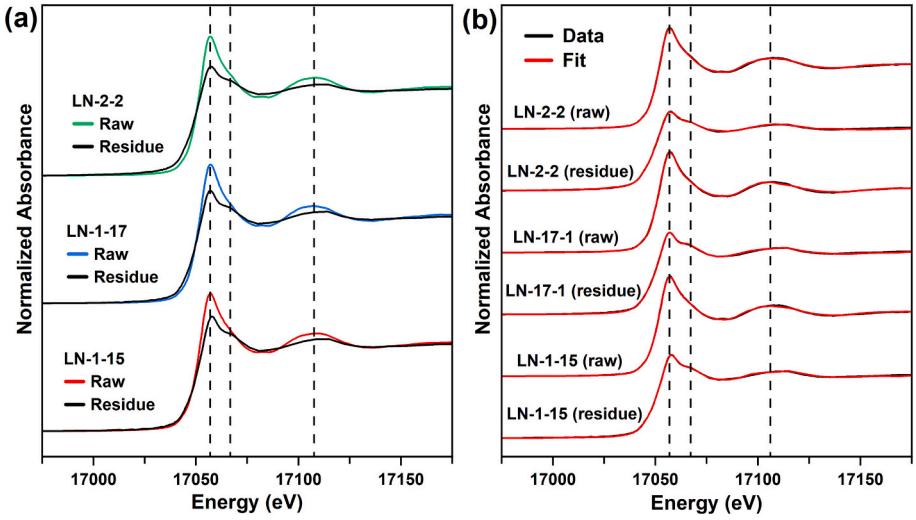

Fig. 3. (a) The overlaid Y bulk XANES spectra and (b) the fitted curves of Type-1 materials and their ion-exchange residues.

Table 4
Bulk XANES Y Speciation of Type-2 materials determined by LCF (errors in parentheses).

Sample	Bulk Y (ppm)	Y Speciation%							
		Y-adsorbed kaolinite	Y-bearing phosphates			Y-bearing hematite	Y-bearing zircon	Sum	R-Factor
			Y-bearing monazite	Y-bearing xenotime	Y-bearing apatite				
K1 raw	27	52.5 (1.7)	21.5 (0.9)	10.4 (1.1)	15.9 (1.2)			100.3	0.0007563
K2 residue	15	20.4 (1.3)	36.7 (1.6)	21.2 (1.4)	21.9 (1.8)			100.2	0.0007052
K3 raw	56	56.3 (1.9)		16.7 (1.2)		14.3 (1.3)	12.8 (0.8)	100.1	0.0008890
K4 residue	36	26.5 (1.7)		26.6 (1.8)		22.4 (1.5)	24.8 (1.6)	100.3	0.0009147
K5 raw	22	8.7 (0.7)	42.7 (1.7)		30.7 (1.9)		17.9 (0.9)	100.0	0.0007218
K6 raw	10	61.8 (1.9)	19.4 (1.2)	11.3 (1.6)			7.7 (0.8)	100.2	0.0008792

zircon (17.9%) and Y-adsorbed kaolinite (<10% Table 4, Fig. 4b). Y speciation in the raw sample from the upper kaolin zone (noted as K6) comprises 61.8% of Y-adsorbed kaolinite, 19.4% of monazite, and 11.3% xenotime. The relative intensity of the main absorption peak (~17,056 eV) compared to the shoulder in the XANES spectrum of K5 appears to be lower than that of K6, which was likely due to the presence of 30.7% of Y in apatite in K5 that has a weaker expression of the main absorption peak compared to monazite and xenotime (~17,056 eV, see Fig. S1 and S2).

3.4. Type-3 sand fractions of bauxite-kaolin samples

3.4.1. Bulk XANES

Y speciation was determined from bulk XANES analyses and LCF

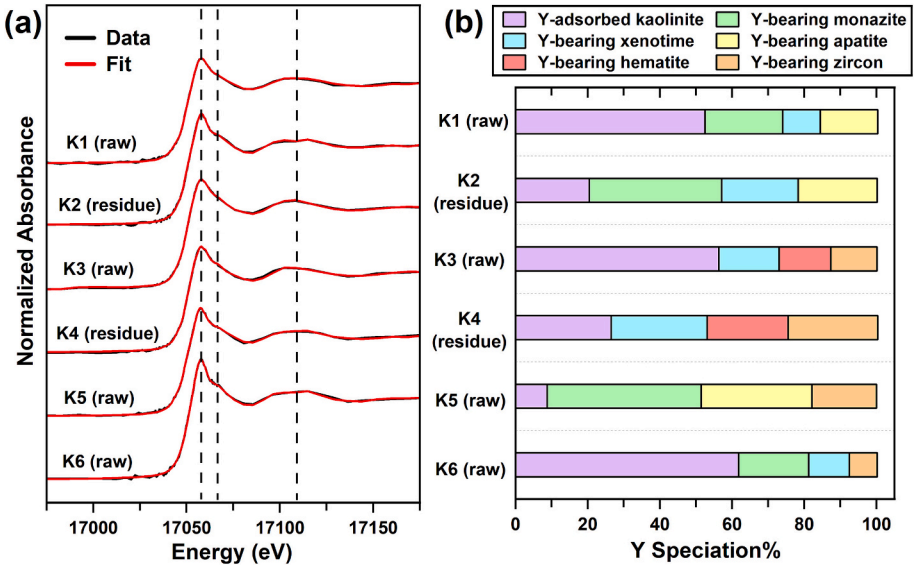

Fig. 4. (a) Y bulk XANES spectra and fitted curves of Type-2 materials, and (b) fractions of Y speciation predicted by LCF.

model analyses for 8 sand fractions separated from clay-rich, bauxite-kaolin materials (Table 1). These sand fractions were previously studied for their non-clay mineral contents (Ashcraft, 2025). Heavy subfractions ("HF", Table 1) from these materials showed varying amounts of Ti-minerals (rutile, ilmenite), zircon, Y-bearing minerals (monazite, xenotime), as well as Fe-sulfides and Fe-oxides. The bulk XANES spectra of Type-3 materials showed a strong absorption peak (~17,056 eV) followed by a clear shoulder (~17,066 eV) and a bimodal hump (~17,108 eV; Fig. S1). Y was speciated nearly exclusively with Y-bearing xenotime (~53–78%) and lesser amounts of Y-bearing monazite (~16–30%), as well as minor amounts of zircon (~7–19%; Fig. 5a, Table 5). Other mineral phases including hematite, kaolinite, and bastnaesite were also predicted by the LCF model to represent a trace amount of Y. However, these phases contributed to less than 5% of Y speciation. Given the typical 10% error range of LCF of XANES data, such a low percentage is not considered statistically reliable. Overall, the average Y speciation in these clay-deficient samples was drastically different from those in Type-2, whole rock bauxite-kaolin samples (Fig. 4b vs. Fig. 5b).

3.4.2. *Micro-XRF/XANES*

To take a closer look at the micro-scale speciation of Y in the Type-3 materials, select samples were characterized by μ-XRF mapping and μ-XANES analyses of thin sections. These samples included G6 (lower kaolin zone), G7 (bauxite zone), and G10 (upper kaolin zone). Sample G11 (Buffalo Creek Member) was also included for comparison.

Mapping included LREE, such as Ce, which proved to be ineffective for locating LREE-associated, Y-bearing particles of interests (POI) due to significant X-ray fluorescence line interferences between Ce Lα (~4.84 keV) and non-REE elements including Ti Kβ (~4.93 keV; Fig. S7). Monazite was the most common LREE+Y-bearing mineral in these samples and contained Ce (~25 wt%), with lesser amounts of P (~12 wt%) and Nd (~11 wt%), but only minor amounts of Y (~3 wt%; Boxleiter and Elliott, 2023). The detection of Ce is known to be more difficult given the co-occurrence of Ce-bearing minerals in geological samples with mineral assemblages containing Ti-minerals (Li et al., 2023). These Type-3 materials contain abundant Ti-minerals (rutile, ilmenite; Ashcraft, 2025), and the difficulty in detecting Ce was therefore not surprising. However, Nd was noted as a potential alternative for

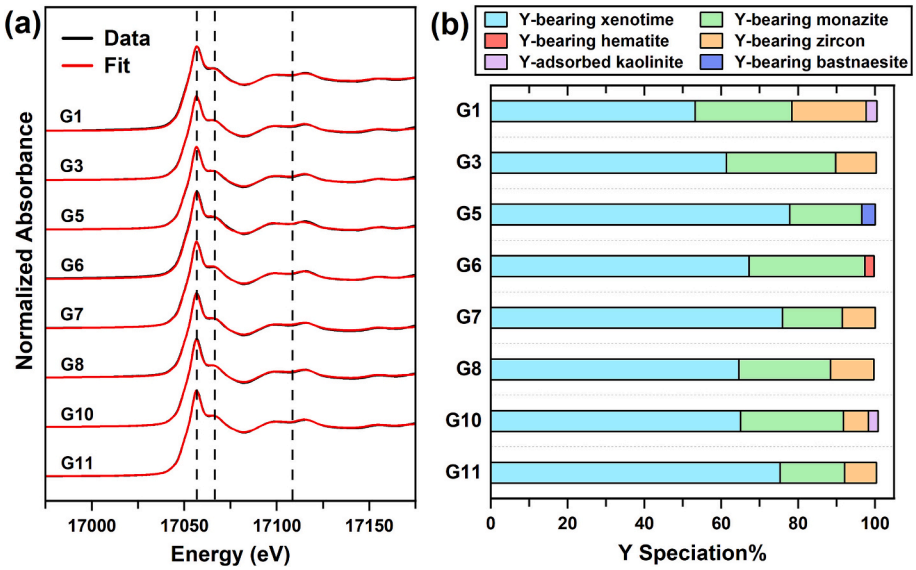

Fig. 5. (a) Y bulk XANES spectra and fitted curves of Type-3 materials, and (b) fractions of Y speciation predicted by LCF.

Table 5
Bulk XANES Y speciation of Type-3 materials determined by LCF (errors in parentheses).

Sample	Y Speciation%							
	Y-bearing phosphates		Y-bearing hematite	Y-bearing zircon	Y-adsorbed kaolinite	Y-bearing bastnaesite	Sum	R-factor
	Y-bearing xenotime	Y-bearing monazite						
G1	53.2 (2.9)	25.2 (2.6)		19.3 (3.4)	2.8 (1.3)		100.5	0.0005924
G3	61.3 (3.7)	28.5 (3.1)		10.5 (2.8)			100.3	0.0005215
G5	77.8 (2.2)	18.8 (2.2)				3.5 (2.1)	100.1	0.0004486
G6	67.2 (2.9)	30.2 (2.1)	2.4 (1.6)				99.8	0.0007602
G7	75.9 (1.8)	15.6 (1.1)		8.6 (1.2)			100.1	0.0004258
G8	64.6 (3.3)	23.8 (3.1)		11.3 (2.2)			99.5	0.0005812
G10	65.0 (2.9)	26.8 (2.6)		6.5 (1.3)	2.5 (1.6)		100.8	0.0004013
G11	75.3 (1.5)	16.8 (1.1)		8.3 (1.9)			100.4	0.0002324

mapping due to less interference between Nd Lα (~5.23 keV) and Ti Kβ (~4.93 keV). Lastly, P was also considered as a potential non-REE target analyte for μ-XRF mapping, but yielded poor results due to X-ray fluorescence line overlaps between P Kα (~2.01 keV) and Zr Lα (~2.04 keV), considering that zircon (Zr-silicate mineral) is also known and abundant in high amounts in these materials.

Mapping for Y, however, was effective in locating micron-size POI for subsequent μ-XANES (Fig. S6). The μ-XANES data showed that Y was predominantly present as Y-bearing phosphates (~76–100%). This includes Y-bearing xenotime (42–80%), Y-bearing monazite (8–33%), and Y-bearing apatite (7–10%; Fig. 6a, Table 6). The μ-XANES spectra across all samples display a very similar characteristic feature as seen in the bulk XANES spectra due to the high contents of Y-bearing xenotime and Y-bearing monazite (Fig. 5a vs. Fig. 6a). The phosphate mineral phases and their μ-XANES spectra were difficult to exclusively fit from one another, even for individual grains, due to strong similarities in the main absorption peak, shoulder, and hump regions (Fig. S1).

Other trace spectral signatures included Y oxide, Y-bearing zircon, and Y-adsorbed ferrihydrite comprising less than 25% of the modelled Y speciation in total. The prominence of Y-bearing phosphate phases as well as the percentages of Y speciation in these selected POI at the micro-scale are consistent with the bulk XANES results illustrated above, especially for samples G6, G7, and G10 (Table 5 vs. Table 6; Fig. 5b vs. Fig. 6b). Notably, the percentage of Y speciation of the selected POI in G11 was markedly different from its corresponding XANES on the bulk sample for G11. The average Y speciation in G11 was composed of Y-bearing xenotime (75.3%), Y-bearing monazite (16.8%), and Y-bearing zircon (8.3%), whereas the selected POI contained Y-bearing xenotime (42.2%), Y-bearing monazite (33.4%), Y oxide (13.3%), and Y-adsorbed ferrihydrite (11.2%).

4. Discussion

4.1. Combined mineralogy and XANES analyses

4.1.1. Type-1 materials

The dominant presence of Y in the Type-1 materials as adsorbed species was consistent with typical Y speciation in weathered, granite-regolith deposits of East Asia (Li et al., 2019, 2020). The results for these Type-1 materials suggested that most of the loosely bound Y (i.e., surface adsorbed Y) were indeed easily extracted through ion-exchange. Following ion-exchange, the residues indicated drastically lower fractions of Y-adsorbed species (i.e. Y-adsorbed kaolinite and ferrihydrite) from 88.7–89.5% (raw sample) to 33.7–37.0% (ion-exchange residue; Table 3), indicating that more than half of the bulk Y was ion-exchangeable. This result is consistent with previous sequential extraction analyses that suggested an ion-exchangeable proportion for these samples was ~65% (± 10%; Li et al., 2019).

This present study confirms the easily extractable nature of these regolith-hosted ion-adsorption clay deposits. However, the LCF results from this study suggest that a minor part of the ion-exchangeable Y could be from ferrihydrite, and therefore not all ion-exchangeable Y is exclusively related to kaolinite. The portion of Y associated with ferrihydrite in the ion-exchange residue could possibly be structural-bound or more strongly adsorbed, similar to mechanisms more well understood for other REE, such as Sc, which was found to be associated with generations of goethite precipitation and the dissolution-crystallization reactions occurring in clay-rich laterite profiles overlying regoliths (Chasse et al., 2019). All told, the Fe—Mn oxyhydroxides in the Type-1 materials in this study were previously determined to account for a minor amount of the bulk REE (~5%; Li et al., 2019).

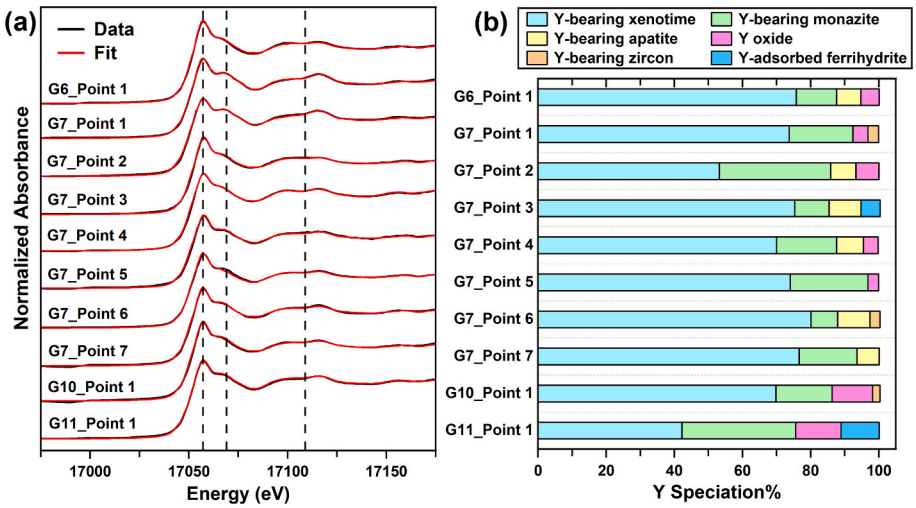

Fig. 6. (a) Y μ-XANES spectra and fitted curves of selected POI from Type-3 materials, and (b) fractions of Y speciation predicted by LCF.

Table 6
μ-XANES Y speciation of Type-3 materials determined by LCF (errors in parentheses).

Sample	Y Speciation%							
	Y-bearing phosphates			Y oxide	Y-bearing zircon	Y-adsorbed ferrihydrite	Sum	R-factor
	Y-bearing xenotime	Y-bearing monazite	Y-bearing apatite					
G6_Point 1	75.8 (2.4)	11.8 (1.5)	7.1 (1.3)	5.4 (1.4)			100.1	0.0007462
G7_Point 1	73.7 (2.0)	18.7 (1.5)		4.4 (1.2)	3.1 (1.2)		99.9	0.0006812
G7_Point 2	53.2 (2.3)	32.7 (2.1)	7.4 (1.4)	6.7 (1.5)			100.0	0.0009570
G7_Point 3	75.3 (2.5)	10.1 (1.5)	9.4 (1.2)			5.6 (1.1)	100.4	0.0008871
G7_Point 4	70.0 (2.2)	17.6 (1.7)	7.9 (1.3)	4.3 (0.9)			99.8	0.0007631
G7_Point 5	74.0 (2.6)	22.8 (2.0)		3.1 (1.8)			99.9	0.0009047
G7_Point 6	80.1 (3.3)	7.8 (2.0)	9.5 (1.8)		2.9 (1.2)		100.3	0.0011933
G7_Point 7	76.6 (2.4)	17.0 (1.8)	6.5 (0.9)				100.1	0.0008827
G10_Point 1	69.8 (2.5)	16.5 (1.6)		11.9 (1.3)	2.1 (1.3)		100.3	0.0009211
G11_Point 1	42.2 (2.1)	33.4 (1.8)		13.3 (0.7)		11.2 (0.9)	100.1	0.0008465

Beyond these minor fractions, the remaining major fractions of Y in the residue were mainly found as Y-bearing apatite, Y-bearing calcite and Y-bearing xenotime. These species combined (sum speciation) increased sharply from ~10–11% (raw sample) to ~63–66% (residual) after ion-exchange, confirming the structural-bound, non-exchangeable nature of Y in these phases. Although apatite was not reported in the Zudong regoliths, the occurrence of some apatite in the bedrocks (Fan et al., 2023; Huang et al., 1989) suggests the possibility of apatite representing a relict phase in the less weathered saprolite. Heterogeneous distribution of these minerals may account for the detection of these mineral phases in the LCF analysis but not in our previous petrographic examination. Alternatively, the apatite could be a neoformed phase during ion-exchange when the exchanged Y precipitated in the circumneutral leaching environment (e.g. Ca and P contents, presumably sourced from the clay minerals and/or poorly crystalline phases). Likewise, that may explain the exceptionally high proportion of Y in Y-bearing calcite in sample LN17–1 after ion-exchange. Nevertheless, further investigation is needed to verify these hypotheses.

Interesting, a previous study identified Y-bearing chernovite ($YAsO_4$) as a common supergene Y-bearing mineral in the Zudong deposit (Li et al., 2019). However, XANES spectrum references are not available in the literature and prevents the determination of this potential candidate to the LCF analysis. Nonetheless, the structural similarity between xenotime and chernovite suggests likely that "Y-bearing xenotime" speciation in these LCF results indeed are largely referring to chernovite. This also matches with the estimated chernovite-hosted REE proportion of 12 ± 8% to 20 ± 6% in upper C and lower B horizons (Li et al., 2019).

4.1.2. Type-2 materials

Overall, the major speciation of Y-adsorbed kaolinite predicted by LCF modeling in the raw bauxite-kaolin samples was consistent with previous findings by Boxleiter et al. (2024). The LCF data also showed higher percentages of Y-adsorbed kaolinite associated with higher kaolinite mineral content in the bulk samples prior to ion-exchange. These LCF data correlated positively with ion-exchangeable Y values found across the geologic section (Boxleiter et al., 2024). Samples K1, K3, and K6 were measured with high kaolinite mineral contents (~72–93 wt%), and the LCF model results suggested that 52.5–61.8% of Y in these samples was primarily present as Y-adsorbed kaolinite (Table 4). On the other hand, sample K5 collected at the top of the bauxite zone has a relatively low kaolinite mineral content (31 wt%) and only contains minor Y-adsorbed kaolinite (8.7%). The majority of Y in sample K5 was hosted by heavy-mineral phases such as Y-bearing phosphates and Y-bearing zircon (Table 4).

4.1.3. Type-3 materials

4.1.3.1. Bulk XANES. The bulk Y speciation in the clay-deficient Type-3 materials (sand fraction samples) was drastically different from the clay-rich Type-2 materials (Fig. 4b vs. Fig. 5b). Comparatively, Y-adsorbed kaolinite comprised up to ~50% of Y speciation in the clay-rich Type-2 materials, whereas heavy-minerals such as Y-bearing phosphates (monazite, xenotime) and zircon are the primary Y hosts for clay-deficient Type-3 materials. These findings are consistent when conjoining the results of other mineralogical datasets from previous studies. For example, xenotime (major) and monazite (minor) were characterized by previous XRD analyses, chemical analyses, and electron microscopy examinations which found these phases to account for the bulk of the Y. The Y was also found enriched in the sand-size (non-clay) fractions from mined kaolin ores in the Upper Coastal Plain including those from the Cretaceous age Buffalo Creek Member, Gaillard Formation (Table 7; Elliott et al., 2018). Moreover, these fractions were known to be enriched in the Y owing to their greater contents of xenotime (HREE-rich phosphate) compared to monazite (LREE-rich phosphate).

LCF results from bulk XANES showed zircon conspicuously accounting for 6.5–19.3% of Y (Table 5). Zircon is a silicate mineral containing significantly less structurally-bound Y compared to phosphate minerals monazite and xenotime. Y contents were ~ 0.087 wt% for Coastal Plain zircons as determined from a bulk mineral concentrate analyses of separated Ti—Zr sands from coastal heavy-mineral deposits (Oladeni, 2022). Comparatively, Y contents were 2.75 wt% from Coastal Plain monazite concentrates derived also from these separated Ti—Zr sands (Oladeni, 2022). These values for monazite were consistent with previous electron microscopy examinations of monazite grains from the Coastal Plain showing Y contents ranging from 2.87 to 3.62 wt% Y (Boxleiter and Elliott, 2023). Considering that Coastal Plain xenotime grains collected from the same rocks contained 28.03–32.92 wt% Y, xenotime followed by monazite will have substantially greater contribution to bulk Y contents. Hypothetically, zircon should be negligible in contribution to the Y contents of the bulk heavy fraction due to very little structural Y. Yet, the total zircon mineral contents were 5–10 times higher than sum of xenotime and monazite for these materials (Table 7),

Table 7
Mineralogy-estimated Y-speciation vs. LCF-predicted Y-speciation. References: (1) Boxleiter and Elliott (2023); (2) Oladeni (2022); (3) Elliott et al. (2018).

	Y-minerals			Sum
	xenotime	monazite	zircon	
Buffalo Creek Heavy Fraction				
structural Y contents, wt.% (1,2)	~31	~3	0.087	NA
mineral contents, wt.% (1,3)	0.6298	0.2467	13.08	13.96
Est. Y contribution to bulk, wt.%	0.1952	0.0076	0.0114	0.2143
Measured Y of bulk, wt.% (3)	NA	NA	NA	0.2175
Est. Y-speciation, wt.%	*91.12*	*3.57*	*5.31*	*100*
Kaolin mine tailings (1)				
structural Y contents, wt.% (1,2)	~31	~3	0.087	NA
mineral contents, wt.% (1)	0.2880	0.9992	4.500	5.7872
Est. Y contribution to bulk, wt.%	0.0893	0.0310	0.0039	0.1242
Measured Y of bulk, wt.% (1)	NA	NA	NA	0.1109
Est. Y-speciation, wt.%	*71.90*	*24.95*	*3.15*	*100*

and therefore these higher abundance of zircon mineral contents in these heavy fractions allows for considering a result of 6.5–19.3% Y-bearing zircon to be reasonable.

Here, for comparison, we quantitatively estimated the Y speciation in the sand-size heavy fractions based on mineral content and the carrying capacity of structural-bound Y for these primary Y phases in the Type-3 materials: xenotime, monazite, and zircon. This estimate was then compared to the measured predictions by XANES and LCF. The estimations of Y speciation were derived from the Y content of each mineral phase contributing to the bulk heavy fraction, divided by the sum Y contents of the bulk heavy fraction. Each mineral phase's contribution of Y was determined by the mineral phase contents (wt%) of the bulk heavy fraction, multiplied by the respective phase's Y contents (wt%).

Using mineralogy from two example specimens of Coastal Plain xenotime-monazite-zircon mixtures, the mineralogy-estimated Y speciation for xenotime was ~70–90% and in somewhat agreement with the LCF-predicted range of 53.2–77.8% (Table 5 vs. Table 7). For monazite these values were ~ 3–25% (mineralogy-estimated) and 15.6–30.2% (LCF predicted). Zircon values were ~ 3–5% (mineralogy-estimated) and 6.5–19.3% (LCF predicted). Therefore, the results from LCF showing 6.5–19.3% of Y speciation accounted for by zircon were a somewhat reasonable agreement considering these comparisons were made across previous to present studies with different sub-samples from similar ore samples (i.e. similar heavy fractions mineral assemblages). LCF of XANES data for mineral mixtures can therefore be considered a potentially useful predictor of mineralogy. These insights contribute to a more comprehensive approach to characterizing the sand fractions derived from mine kaolins and bauxites and their Y contents.

4.1.3.2. Micro XANES. It is noteworthy that μ-XANES results reflect spatially resolved information by focusing on individual Y-bearing grains identified by μ-XRF, whereas bulk XANES results represent the average signals across the entire sample. Insights provided by bulk XANES and μ-XRF/μ-XANES analyses complement each other to enable a more comprehensive understanding of the speciation of target elements in the samples. Natural rock samples are often heterogeneous, containing a mixture of multiple mineral phases as well as chemically distinct micro-inclusions, grain boundaries, and secondary crystal overgrowths. For heterogeneous samples with a complex matrix, the local Y speciation revealed by μ-XANES could differ from the average Y speciation suggested by bulk XANES depending on the percent distribution, which was observed in our previous study on REE speciation in coal fly ash (Wen et al., 2025). As shown in Table 6, some minor Y-bearing phases (e.g., Y-bearing apatite, Y oxide, and Y-adsorbed ferrihydrite) identified by μ-XRF/μ-XANES are not representative of the bulk Y speciation (Table 5). Nevertheless, LCF results from both bulk and μ-XANES corroborate that Y-bearing phosphate minerals, including xenotime and monazite, are the predominant Y-bearing phases in the heavy fractions bauxite-kaolin samples.

4.2. Implications to the supergene REE mobilization and enrichment processes

4.2.1. Regolith-hosted ion-adsorption REE ore formation

In this study, the Type-1 materials represent regolith-hosted ion-adsorption REE ores at different pedological stages: LN-2-2 from the lower B horizon, LN-17-1 from the upper C horizon, and LN-1-15 from a relatively lower depth in the C horizon. All the samples are characterized by a high proportion of Y adsorbed on kaolinite and ferrihydrite (~90%), defining the ion-adsorption nature of the ore with highly ion-exchangeable total REE contents (~50–70%). In agreement with other similar deposits in South China, kaolinite was confirmed to be a main sorbent for the ion-exchangeable REE (Li and Zhou, 2020, 2023; Wang et al., 2024). Notably, the proportion of Y adsorbed on ferrihydrite decreases from the C to B horizon, suggesting a more important role of ferrihydrite in adsorbing REE in a less weathered, higher pH environment (Liang et al., 2025). With progressive weathering, the metastable ferrihydrite would gradually re-crystallize to more crystalline goethite and hematite (Schwertmann and Murad, 1983; Das et al., 2011; Yang et al., 2021) and thereby may lose the ability for REE adsorption (Liang et al., 2025). On the other hand, the increase in the proportion of Y-bearing xenotime indicates a residual accumulation to certain extent by relict xenotime, and likely supergene chernovite during progressive weathering as well (cf. Li et al., 2019). Relict apatite may account for a minor portion of the REE in the slightly to moderately weathered materials in the lower B and upper C horizons, while under more intense weathering, they should completely dissolve and become absent from the regoliths (cf. Li et al., 2022).

4.2.2. Sedimentary-hosted REE mineralization

Findings of this study are notably consistent with the geology of the Georgia bauxite-kaolin deposit (Boxleiter et al., 2024). High amounts of Y-adsorbed kaolinite (~52–62%) per XANES-LCF and high amounts of ion-exchangeable Y were found above (12.3%) and below (~33–36%) the bauxite zone. The top of the bauxite zone (noted as K5, Table 1) contained the lowest amounts of Y-adsorbed kaolinite (8.7%) and ion-exchangeable Y (<5%). The Y contents of the top of the bauxite zone were primarily associated with residual phases such as Y-phosphates and zircon (Table 4). The occurrence of high amounts of Y adsorbed on kaolinite and overall highest ion-exchangeable Y contents were found in strata underlying the bauxite zone. The accumulation of Y in these strata underlying the bauxite zone was attributed to the movement of dissolved Y and other REE from the zone of bauxitization (laterization). During bauxitization, kaolinite underwent chemical weathering and conversion to gibbsite with lower sorption capacity compared to kaolinite. These remobilized Y were sorbed on to kaolinite mineral surfaces leading to sizable Y-adsorbed kaolinite and ion-exchangeable Y contents. These contents were found near the stratigraphic transition between the bauxite zone (up to 67 wt% gibbsite) and the underlying lower kaolin zone strata with ≤5 wt. gibbsite.

Concomitantly, the Y in the sand-size grains are predominately associated with xenotime, and subordinately by monazite followed by zircon. Both xenotime ($\rho = 4.8–5.5$ g/cm^3) and monazite ($\rho = 4.4–5.1$ g/cm^3) are concentrated in the heavy-mineral assemblages by natural processes and deposited (e.g. hydrologic, mechanical sorting; Bern et al., 2016). Post-depositional alteration caused partial dissolution of these phases for secondary mineralization of fine-grained LREE-phosphates (Cheshire, 2011) and possibly contributing to the ion-adsorption mineralization in the kaolins (Boxleiter and Elliott, 2023).

4.2.3. Feasible methods for effective extraction

Extraction of Y and other REE from regolith-hosted ores (noted as Type-1 materials) will likely continue to be derived from in-situ leaching methods. Type-1 materials contain the largest portion (~50–70%) of their sum REE contents in an exchangeable form as shown by high Y-adsorbed clay and iron oxyhydroxide mineral contents. Given the in-situ nature of current leach-mining practices, it seems feasible to also consider in-situ technologies for second-stage extractions. The second stage extraction could target the minor remaining portions (<25%, bulk REE) associated with Y-bearing phosphates, Y-bearing silicates, and possible Y-bearing carbonates. While REE substituted in these mineral phases cannot be easily released via ion-exchange, our recent studies found that green organic acids (e.g., citric acid) are effective in REE extraction due to their strong metal-complexing ability without relying on use of concentrated strong inorganic acids (e.g., HCl) (Wen et al., 2023; Wen et al., 2024). However, more efforts are needed to evaluate the techno-economic feasibility of second-stage extraction.

Comparatively, effective extraction of Y and other REE from sedimentary-hosted ores and their waste streams (i.e. mine tailings), noted as Type-2 and Type-3 materials, may look completely different. The bauxite-kaolin ores (Type-2 materials) are presently mined for the

wide range in traditional kaolin-clay usage, as well as bauxites used by the refractories industry. Heap-leaching of low-grade ores not produced to market could be considered for their quantities of exchangeable REE, albeit their lower exchangeable and lower bulk REE contents indicate different economics than Type-1 materials. Type-3 materials on the other-hand are treated as mine waste tailings. Mined kaolins are processed by screening and density-based separations which separate the kaolin-clay and non-clay (sandy gangue, or "grit" – Type-3 material). These Type-3 materials contain significant fractions of HREE associated primarily with a xenotime and monazite (Elliott et al., 2018). Considering that these Type-3 materials represent waste streams from active mining operations that are moved and impounded (back-filled) into abandoned mine pits, the potential of batch processing for REE recovery is an attractive proposition and deserves further consideration.

5. Conclusions

In this study, X-ray absorption spectroscopy was able to distinguish between Y-adsorbed species and lattice-bound Y in phosphates, silicates, and other minerals. Previous studies were able to make these and similar distinctions in REE speciation based on pure and/or lab-doped reference compounds. This present study was able to demonstrate the usefulness X-ray absorption near-edge spectroscopy (XANES) paired with linear combination fitting (LCF) to quantify the breakdown of Y speciation from natural samples containing a mixture of Y-bearing phases (clay and non-clay minerals). The materials in this study included clay-rich ores (Type-1 and Type-2, bulk samples) and clay-deficient process waste materials (Type-3, grain separates). Comparison of the raw, clay-rich ore samples and their ion-exchange residue fractions confirmed a high proportion of Y existing in ion-exchangeable (Y-adsorbed) form in the Type-1 and Type-2 materials. Meanwhile, heavy minerals such as xenotime, monazite, and zircon were the primary hosts of Y (lattice-bound) in the Type-3 materials.

Given the differences in extractability between ion-adsorbed clays and non-clay Y-bearing minerals such as xenotime, monazite, and zircon, the following summary points were highlighted:

1. Augmenting mineralogical datasets with X-ray absorption spectroscopic examination was required to produce a clearer picture of the link between the mineralogical profile (mineral assemblage) and the chemical profile (elemental speciation) of ore deposits and their processed fractions.
2. Demonstrating the usefulness of applying X-ray absorption spectroscopy techniques to study Y speciation was expanded beyond the characterization of pure and/or lab-doped reference compounds. This present study showed that XANES paired with LCF can be effective in quantifying the breakdown of Y speciation from bulk mixtures (natural ore samples) containing multiple phases and modes of occurrence (adsorbed vs. lattice-bound speciation).
3. The recovery of Y and other REE from ores and their waste streams will continue to depend on their soluble and insoluble fractions yielded by any given extraction technology, such as conventional ion-exchange treatments for ion-adsorption clays. Therefore, evaluating prospective rare earth feedstocks would benefit greatly from X-ray absorption spectroscopic characterizations involving the techniques explored in this study.

CRediT authorship contribution statement

Anthony Boxleiter: Writing – review & editing, Writing – original draft, Resources, Methodology, Investigation, Formal analysis, Data curation, Conceptualization. **Yinghao Wen:** Writing – review & editing, Validation, Software, Methodology, Investigation, Formal analysis, Data curation. **Martin Yan Hei Li:** Writing – review & editing, Resources, Investigation, Conceptualization. **Joell Ashcraft:** Resources, Methodology, Investigation, Data curation. **Yuanzhi Tang:** Writing – review & editing, Supervision, Resources, Project administration, Funding acquisition. **W. Crawford Elliott:** Writing – review & editing, Supervision, Resources, Project administration, Funding acquisition.

Declaration of competing interest

The authors declare the following financial interests/personal relationships which may be considered as potential competing interests:

Yuanzhi Tang and W. Crawford Elliott report financial support was provided by National Science Foundation. Anthony Boxleiter reports a relationship with Imerys that includes: employment. W. Crawford Elliott has a patent "Extracting rare earth elements from a gangue heavy fraction", US Patent 10,688,501 and US Patent 12,179,214, issued to Georgia State University Research Foundation, and to Thiele Kaolin Company. Yuanzhi Tang is a current member of the Chemical Geology Editorial Board. If there are other authors, they declare that they have no known competing financial interests or personal relationships that could have appeared to influence the work reported in this paper.

Acknowledgements

This work is supported by National Science Foundation (NSF). Yuanzhi Tang acknowledges support by NSF Grant # 2327660. W. Crawford Elliott acknowledges support by NSF Grant # 2327659. The authors thank the beamline scientists at Beamline 6-BM at National Synchrotron Light Source (NSLS-II) in Brookhaven National Laboratory (Upton, NY) and Beamline 11-2 at the Stanford Synchrotron Radiation Lightsource (SSRL) in the SLAC National Accelerator Laboratory (Menlo Park, CA) for their assistance in instrument setup and data collection. NSLS-II is a U.S. Department of Energy (DOE) Office of Science User Facility operated for the DOE Office of Science by Brookhaven National Laboratory under Contract No. DE-SC0012704. Use of the SSRL, SLAC National Accelerator Laboratory, is supported by the U.S. DOE Office of Science, Office of Basic Energy Sciences under Contract No. DE-AC02-76SF00515. The authors thank Drew Hooper for his preparation of the Buffalo Creek sample which was used in this study. The authors also thank the editor and two anonymous reviewers for their comments and recommendations during revisions.

Appendix A. Supplementary data

Supplementary data to this article can be found online at https://doi.org/10.1016/j.chemgeo.2026.123312.

Data availability

All data used to prepare this paper are given in the text of in the Supplementary Information.

References

Ashcraft, J., 2025. Rare-Earth Elements in the Cretaceous to Eocene Age Bauxite-Kaolin Ores, Upper Coastal Plain, Georgia. Georgia State University. https://doi.org/10.57709/sr1b-h724.

Ashcraft, J., Boxleiter, A., Hooper, D., Wen, Y., Tang, Y., Elliott, W.C., 2025. Rare earth elements in the Cretaceous to Eocene Age Bauxite-Kaolin ores, Upper Coastal Plain, Georgia. Geol. Soc. Am. Abstr. Programs 57 (2). https://doi.org/10.1130/abs/2025SE-408833.

Bao, Z., Zhao, Z., 2008. Geochemistry of mineralization with exchangeable REY in the weathering crusts of granitic rocks in South China. Ore Geol. Rev. 33 (3), 519–535. https://doi.org/10.1016/j.oregeorev.2007.03.005.

Beard, C.D., Marquis, E., Smith, M.P., Li, M.Y.H., Estrade, G., Goodenough, K.M., 2025. Ion adsorption mineralisation in regolith-hosted REE deposits. In: Geology, Geochemistry and Formation of Supergene Mineral Deposits in Deeply Weathered Terrain. Springer Nature Switzerland, Cham, pp. 365–394. https://doi.org/10.1007/978-3-031-75733-4_14.

Bern, C.R., Shah, A.K., Benzel, W.M., Lowers, H.A., 2016. The distribution and composition of REE-bearing minerals in placers of the Atlantic and Gulf coastal plains, USA. J. Geochem. Explor. 162, 50–61. USGS Publications Warehouse. https://doi.org/10.1016/j.gexplo.2015.12.011.

Bern, C.R., Yesavage, T., Foley, N.K., 2017. Ion-adsorption REEs in regolith of the Liberty Hill pluton, South Carolina, USA: an effect of hydrothermal alteration. J. Geochem. Explor. 172, 29–40. USGS Publications Warehouse. https://doi.org/10.1016/j.gexplo.2016.09.009.

Bishop, B.A., Alam, Md.S., Flynn, S.L., Chen, N., Hao, W., Ramachandran Shivakumar, K., Swaren, L., Gutierrez Rueda, D., Konhauser, K.O., Alessi, D.S., Robbins, L.J., 2024. Rare earth element adsorption to clay minerals: mechanistic insights and implications for recovery from secondary sources. Environ. Sci. Technol. 58 (16), 7217–7227. https://doi.org/10.1021/acs.est.4c00974.

Borst, A., Smith, M., Finch, A., Estrade, G., Villanova-de-Benavent, C., Nason, P., Marquis, E., Goodenough, K., Xu, C., Kynicky, J., Geraki, K., 2020. Adsorption of rare earth elements in regolith-hosted clay deposits. Nat. Commun. 11. https://doi.org/10.1038/s41467-020-17801-5.

Boxleiter, A., Elliott, W.C., 2023. Rare-earth minerals in kaolin ore, mine tailings, and sands – Central Georgia, Upper Coastal Plain. Clays Clay Miner. 71 (3), 274–308. https://doi.org/10.1007/s42860-023-00235-7.

Boxleiter, A., Wen, Y., Tang, Y., Elliott, W.C., 2024. Rare-earth element (REE) remobilization and fractionation in bauxite zones from sedimentary kaolin deposits, western Georgia (USA), upper Coastal Plain. Chem. Geol. 660, 122151. https://doi.org/10.1016/j.chemgeo.2024.122151.

Brahim, J.A., Hak, S.A., Achiou, B., Boulif, R., Beniazza, R., Benhida, R., 2022. Kinetics and mechanisms of leaching of rare earth elements from secondary resources. Miner. Eng. 177, 107351. https://doi.org/10.1016/j.mineng.2021.107351.

Bunzli, J.-C.G., 2013. Lanthanides. In: Kirk-Othmer Encyclopedia of Chemical Technology, pp. 1–43. https://doi.org/10.1002/0471238961.1201142019010215.a01.pub3.

Chasse, M., Griffin, W.L., O'Reilly, S.Y., Calas, G., 2019. Australian laterites reveal mechanisms governing scandium dynamics in the critical zone. Geochim. Cosmochim. Acta 260, 292–310. https://doi.org/10.1016/j.gca.2019.06.036.

Cheshire, M., 2011. Isotopic and Geochemical Composition of the Georgia Kaolins: Insights into Formation and Diagenetic Conditions. Indiana University.

Cheshire, M., Bish, D., Cahill, J., Kertesz, V., Stack, A., 2018. Geochemical evidence for rare-earth element mobilization during kaolin diagenesis. ACS Earth Space Chem. 2. https://doi.org/10.1021/acsearthspacechem.7b00124.

Das, S., Hendry, M.J., Essilfie-Dughan, J., 2011. Transformation of two-line ferrihydrite to goethite and hematite as a function of pH and temperature. Environ. Sci. Technol. 45, 268–275. https://doi.org/10.1021/es101903y.

Elliott, W.C., Gardner, D.J., Malla, P., Riley, E.D., 2018. A new look at the occurrences of the rare-earth elements in the Georgia Kaolins. Clays Clay Miner. 66, 245–260. https://doi.org/10.1346/CCMN.2018.064096.

Fan, C., Xu, C., Shi, A., Smith, M.P., Kynicky, J., Wei, C., 2023. Origin of heavy rare earth elements in highly fractionated peraluminous granites. Geochim. Cosmochim. Acta 343, 371–383. https://doi.org/10.1016/j.gca.2022.12.019.

He, Z., Zhang, Z., Yu, J., Zhou, F., Xu, Y., Xu, Z., Chen, Z., Chi, R., 2016. Kinetics of column leaching of rare earth and aluminum from weathered crust elution-deposited rare earth ore with ammonium salt solutions. Hydrometallurgy 163, 33–39. https://doi.org/10.1016/j.hydromet.2016.02.016.

Huang, D., Wu, C., Han, J., 1989. REE geochemistry and mineralization characteristics of the Zudong and Guanxi granites, Jiangxi Province. Acta Geol. Sin. 2, 139–157. https://doi.org/10.1111/j.1755-6724.1989.mp2002004.x.

Langmuir, D., 1997. Aqueous Environmental Geochemistry (1st ed.). Pearson.

Li, M.Y.H., Zhou, M.-F., 2020. The role of clay minerals in forming the regolith-hosted heavy rare earth element deposits. Am. Mineral. 105, 92–108. https://doi.org/10.2138/am-2020-7061.

Li, M.Y.H., Zhou, M.F., 2023. Physicochemical variation of clay minerals and enrichment of rare earth elements in regolith-hosted deposits: exemplification from the Bankeng Deposit in South China. Clays Clay Miner. 71 (3), 362–376. https://doi.org/10.1007/s42860-023-00250-8.

Li, Y.H.M., Zhao, W.W., Zhou, M.-F., 2017. Nature of parent rocks, mineralization styles and ore genesis of regolith-hosted REE deposits in South China: an integrated genetic model. J. Asian Earth Sci. 148, 65–95. https://doi.org/10.1016/j.jseaes.2017.08.004.

Li, M.Y.H., Zhou, M.-F., Williams-Jones, A.E., 2019. The genesis of regolith-hosted heavy rare earth element deposits: insights from the World-Class Zudong Deposit in Jiangxi Province, South China. Econ. Geol. 114 (3), 541–568. https://doi.org/10.5382/econgeo.4642.

Li, M.Y.H., Zhou, M.F., Williams-Jones, A.E., 2020. Controls on the dynamics of rare earth elements during subtropical hillslope processes and formation of regolith-hosted deposits. Econ. Geol. 115 (5), 1097–1118. https://doi.org/10.5382/econgeo.4727.

Li, M.Y.H., Kwong, H.T., Williams-Jones, A.E., Zhou, M.-F., 2022. The thermodynamics of rare earth element liberation, mobilization and supergene enrichment during groundwater-regolith interaction. Geochim. Cosmochim. Acta 330, 258–277. https://doi.org/10.1016/j.gca.2021.05.002.

Li, W., Yamada, S., Hashimoto, T., Okumura, T., Hayakawa, R., Nitta, K., Sekizawa, O., Suga, H., Uruga, T., Ichinohe, Y., Sato, T., Toyama, Y., Noda, H., Isobe, T., Takatori, S., Hiraki, T., Tatsuno, H., Kominato, N., Ito, M., Takahashi, Y., 2023. High-sensitive XANES analysis at Ce L2-edge for Ce in bauxites using transition-edge sensors: implications for Ti-rich geological samples. Anal. Chim. Acta 1240, 340755. https://doi.org/10.1016/j.aca.2022.340755.

Liang, X., Wu, P., Wei, G., Yang, Y., Ji, S., Ma, L., Zhou, J., Tan, W., Zhu, J., Takahashi, Y., 2025. Enrichment and fractionation of rare earth elements (REEs) in ion-adsorption-type REE deposits: constraints of an iron (hydr)oxide-clay mineral composite. Am. Mineral. 110 (1), 114–135. https://doi.org/10.2138/am-2023-9217.

Liu, P., Huang, R., Tang, Y., 2019. Comprehensive understandings of rare earth element (REE) speciation in coal fly ashes and implication for REE extractability. Environ. Sci. Technol. 53 (9), 5369–5377. https://doi.org/10.1021/acs.est.9b00005.

Long, K., Gosen, B.S., Foley, N., Cordier, D., 2010. The principal rare earth elements deposits of the United States. In: USGS Scientific Investigations Report 2010-5220, p. 96. http://pubs.usgs.gov/sir/2010/5220/.

Long, P., Wang, G., Zhang, C., Yang, Y., Cao, X., Shi, Z., 2020. Kinetics model for leaching of ion-adsorption type rare earth ores. J. Rare Earths 38 (12), 1354–1360. https://doi.org/10.1016/j.jre.2019.11.011.

Maurice, P., 2009. Environmental Surfaces and Interfaces from the Nanoscale to the Global Scale. Wiley. https://books.google.com/books?id=92ovAQAAIAAJ.

Moldoveanu, G.A., Papangelakis, V.G., 2012. Recovery of rare earth elements adsorbed on clay minerals: I. Desorption mechanism. Hydrometallurgy 117–118, 71–78. https://doi.org/10.1016/j.hydromet.2012.02.007.

Moldoveanu, G.A., Papangelakis, V.G., 2013. Recovery of rare earth elements adsorbed on clay minerals: II. Leaching with ammonium sulfate. Hydrometallurgy 131–132, 158–166. https://doi.org/10.1016/j.hydromet.2012.10.011.

Moldoveanu, G., Papangelakis, V., 2016. An overview of rare-earth recovery by ion-exchange leaching from ion-adsorption clays of various origins. Mineral. Mag. 80, 63–76. https://doi.org/10.1180/minmag.2016.080.051.

Oladeni, I., 2022. Rare-earth Element Occurrences in Heavy Mineral Sand, Southeast Georgia. Thesis. Georgia State University. https://doi.org/10.57709/28900383.

Ruan, C., Jun, T., 2011. Weathered crust elution deposited rare earth ores. In: Weathered Crust Elution deposited Rare Earth Ores, pp. 1–308.

Ruan, C., Jun, T., Zhongjun, L., Cui, P., Yuanxin, W., Shirong, L., Cunwen, W., Zhou, Z.A., 2005. Existing state and partitioning of rare earth on weathered ores. J. Rare Earths 23, 756–759.

Sanematsu, K., Watanabe, Y., 2016. Characteristics and genesis of ion adsorption-type rare earth element deposits. In: Verplanck, P.L., Hitzman, M.W. (Eds.), Rare Earth and Critical Elements in Ore Deposits, 18. Society of Economic Geologists, pp. 55–79. https://doi.org/10.5382/Rev.18.03.

Schwertmann, U., Murad, E., 1983. Effect of pH on the formation of goethite and hematite from ferrihydrite. Clay Clay Miner. 31, 277–284. https://doi.org/10.1346/CCMN.1983.0310405.

Taggart, R.K., Rivera, N.A., Levard, C., Ambrosi, J.-P., Borschneck, D., Hower, J.C., Hsu-Kim, H., 2018. Differences in bulk and microscale yttrium speciation in coal combustion fly ash. Environ. Sci. 20 (10), 1390–1403. https://doi.org/10.1039/C8EM00264A.

Tanaka, K., Takahashi, Y., Shimizu, H., 2008. Local structure of Y and Ho in calcite and its relevance to Y fractionation from Ho in partitioning between calcite and aqueous solution. Chem. Geol. 248 (1), 104–113. https://doi.org/10.1016/j.chemgeo.2007.11.003.

Van Gosen, B.S., Verplanck, P.L., Emsbo, P., 2019. Rare earth element mineral deposits in the United States, 24. USGS Publications Warehouse. https://doi.org/10.3133/cir1454.

Verplanck, P., 2017. The role of fluids in the formation of rare earth element deposits. Proc. Earth Planet. Sci. 17, 758–761. https://doi.org/10.1016/j.proeps.2017.01.014.

Wang, Z., Li, M.Y.H., Liu, Z., Zhou, M.-F., 2021. Scandium: ore deposits, the pivotal role of magmatic enrichment and future exploration. Ore Geol. Rev. 128, 103906. https://doi.org/10.1016/j.oregeorev.2020.103906.

Wang, M., Li, M.Y.H., Zhou, M.F., Zhou, J.X., Sun, G., Zhou, Y., Li, Y., 2024. Enrichment of rare earth elements during the weathering of alkaline igneous systems: insights from the Puxiong regolith-hosted rare earth element deposit, SW China. Econ. Geol. 119 (1), 161–187. https://doi.org/10.5382/econgeo.5024.

Wen, Y., Hu, L., Boxleiter, A., Li, D., Tang, Y., 2023. Rare earth elements recovery and waste management of municipal solid waste incineration ash. ACS Sustain. Resour. Manag. 1 (1), 17–27. https://doi.org/10.1021/acssusresmgt.3c00026.

Wen, Y., Liu, P., Wang, Q., Zhao, S., Tang, Y., 2024. Organic ligand-mediated dissolution and fractionation of rare-earth elements (REEs) from carbonate and phosphate minerals. ACS Earth Space Chem. 8 (5), 1048–1061.

Wen, Y., Hu, L., Liu, P., Wang, Q., Garcia, E., Yan, W., Tang, Y., 2025. Rare earth element (REE) speciation in municipal solid waste incineration ash. Appl. Geochem. 178, 106239. https://doi.org/10.1016/j.apgeochem.2024.106239.

Wu, C., Huang, D., Guo, Z., 1990. REE geochemistry in the weathered crust of granites, Longnan Area, Jiangxi Province. Acta Geol. Sin. 3 (2), 193–209. https://doi.org/10.1111/j.1755-6724.1990.mp3002006.x.

Wu, C., Yuan, Z., Bai, G., 1996. Rare earth deposits in China. In: Rare Earth Minerals: Chemistry, Origin and Ore Deposits, 7, pp. 281–306.

Xiao, Y., Chen, Y., Feng, Z., Huang, X., Huang, L., Long, Z., Cui, D., 2015. Leaching characteristics of ion-adsorption type rare earths ore with magnesium sulfate. Trans. Nonferrous Met. Soc. Chin. 25 (11), 3784–3790. https://doi.org/10.1016/S1003-6326(15)64022-5.

Xu, C., Kynicky, J., Smith, M., Kopřiva, A., Brtnický, M., Urubek, T., Yang, Y., Zhao, Z., He, C., Wenlei, S., 2017. Origin of heavy rare earth mineralization in South China. Nat. Commun. 8. https://doi.org/10.1038/ncomms14598.

Yang, X.J., Lin, A., Li, X.-L., Wu, Y., Zhou, W., Chen, Z., 2013. China's ion-adsorption rare earth resources, mining consequences and preservation. Environ. Dev. 8, 131–136. https://doi.org/10.1016/j.envdev.2013.03.006.

Yang, M., Liang, X., Li, Y., He, H., Zhu, R., Arai, Y., 2021. Ferrihydrite transformation impacted by adsorption and structural incorporation of rare earth elements. ACS Earth Space Chem. 5 (10), 2768–2777. https://doi.org/10.1021/acsearthspacechem.1c00159.